Multiphysics modeling tool for photovoltaic-thermoelectric hybrid devices integrating a photothermal interface

Sébastien Hanauer, Léopold Boudier, Adnen Mlayah, Inès Revol

Energy Conversion and Management: X 23 (2024) 100665

Contents lists available at ScienceDirect

Energy Conversion and Management: X

journal homepage: www.sciencedirect.com/journal/energy-conversion-and-management-x

Multiphysics modeling tool for photovoltaic-thermoelectric hybrid devices integrating a photothermal interface

Sébastien Hanauer, Léopold Boudier, Adnen Mlayah, Inès Revol *

LAAS-CNRS, Université de Toulouse, CNRS, UPS, Toulouse, France

ARTICLE INFO

Keywords:
Photovoltaic
Thermoelectric
Solar energy conversion
Hybrid devices
Modeling
Photothermal interface

ABSTRACT

Photovoltaic-thermoelectric hybrid devices aim at harvesting the entire solar spectrum via both direct photovoltaic conversion and subsequent thermoelectric conversion of the heat generated in the solar cell. One emerging strategy to improve their efficiency is to implement a photothermal interface between the photovoltaic cell and the thermoelectric module. Modeling such a complex system (photovoltaic cell, photothermal interface and thermoelectric generator) to design an optimal architecture is a challenging task, as it requires to take into account a large number of parameters in a multi-layered system, as well as the coupling between optical, thermal and electrical effects. To do so, we present here a multiphysics tool to predict the temperature distribution and power output of hybrid devices integrating a photothermal interface. Our model shows a good quantitative agreement with previous theoretical and experimental works from the literature using limited material parameters. We discuss the need for additional parameters for accurate modeling of experimental devices. We envision that our multiphysics modeling tool will be key for the design of optimal photothermal interfaces for efficient photovoltaic-thermoelectric hybrid devices.

1. Introduction

A decade ago, photovoltaic-thermoelectric hybrid devices emerged as an innovating approach for solar energy harvesting. To make the most out of solar energy, these hybrid devices combine a solar photovoltaic cell (PVC) with a thermoelectric generator (TEG). Though there is a growing number of experimental demonstrations of PVC-TEG devices with significant gain in conversion efficiency compared to the solar cell alone [1–5], there are still some limitations to the deployment of this technology. One inherent issue is the mismatch between the optimal temperatures of the PVC and the TEG components. Furthermore, the low conversion efficiency of the current TEG devices hinders the benefit of hybridization. As a matter of fact, a critical issue of PVC-TEG devices, though often overlooked, is the physical interface between the solar cell and the TEG. Several works focused on improving the thermal properties of the PVC-TEG interface to reduce the thermal contact resistance [6–11].

To go further, it was suggested to add an optical role to this interface, by using a photothermal material. Such a photothermal interface (PTI) would be able to selectively absorb the near infrared photons that are not used by the solar cell and convert them into heat, thus increasing the temperature at the hot side of the TEG. As the electrical power output of the TEG directly correlates to the temperature difference between its hot and cold side [12], this approach could lead to increase the conversion efficiency of the PVC-TEG device.

A few experimental studies have reported the demonstration of PVC-TEG devices integrating such interfaces combining tailored optical and thermal properties. These studies investigated various designs of thin-film interfaces, including a solar selective absorber made of cermet layers [1], a thin acrylic film dyed with an exothermic reactive aluminum-doped zinc oxide dye [7], a boron nitride layer with reduced graphene oxide [10], carbon paste with or without boron nitride [11], and a metal/ceramic multilayer [13]. Though the integration of a photothermal interface can be beneficial to the hybrid system, the presence of the photothermal interface is also likely to increase the temperature of the photovoltaic cell [10], potentially reducing its performances.

Indeed, it is not certain that the impact of a PTI will be positive on the overall conversion efficiency of the PVC-TEG device. This depends notably on the thermal resistance of the PTI and other components of the system, as well as the heat extraction capacity on the cold side of the TEG [14]. If the thermal resistance of the PTI is too high, it may reduce the heat transfer from the PVC to the TEG, leading to an increase in

* Corresponding author.
E-mail address: ines.revol@laas.fr (I. Revol).

https://doi.org/10.1016/j.ecmx.2024.100665

Available online 19 July 2024

temperature within the PVC and a reduction in temperature at the hot contact of the TEG. When aiming to optimize the design of a PTI, a balance must be struck between its optical and thermal properties. This optimization also depends on the properties of the PVC and the TEG, as well as the environment. Therefore, there are no clear guidelines to design an optimal photothermal interface. We propose to fill this gap in the literature by considering all these parameters in our model, in order to guide the design of optimized PVC-PTI-TEG systems.

So far, there is only one published work addressing the performance prediction of PVC-TEG hybrid devices integrating different thermal interface materials, relying on a machine learning approach [11]. Using an artificial neural network, Park et al. showed a correlation between the output power of the PVC-TEG device and the thermal interface material properties (absorptance, thermal conductivity and light-to-heat conversion factor). However, such an approach requires large sets of experimental data for the training phase (over a hundred in Ref. [11]), which is not always doable. On the other hand, several works have proposed analytical or semi-analytical models to predict the performance of PVC-TEG hybrid devices [15–20]. In most of these models, only the photovoltaic layer is considered as optically active, all other layers being transparent. Zhou and coworkers have elaborated a multiphysics model to study different PVC-TEG devices with a nanostructured front surface [21]. Their model accounts for the presence of two optically active layers (the nanostructured front surface and the photovoltaic active layer) and thus includes the spectral response of the materials. Yet, in this model, only the photovoltaic active layer is able to absorb light.

To our knowledge, so far, none of the reported models includes an optically and thermally active interface between the solar cell and the TEG. Here we present a multiphysics modeling tool conceived to predict the global output power of hybrid energy devices integrating a photothermal interface.

Section 2 of the paper describes the multiphysics model we have built for the PVC-TEG hybrid device, including a comparison of the proposed model with the model from Zhou et al. [21]. Section 3 focuses on the integration of a photothermal interface in the model, the validity of the model being discussed through the comparison with a published experimental study from Park et al. [10]. We show that the multiphysics model presented in this work is a versatile tool and can be used in a straightforward way to assist the design of an optimal photothermal interface for a given PVC-TEG device. This work opens perspectives towards the experimental demonstration of efficient PVC-TEG devices with a fully synergistic hybridization.

2. Building a multiphysics model for the PVC-TEG hybrid device

A photovoltaic-thermoelectric device is a complex system in which optical, thermal and electrical effects are strongly interconnected. As illustrated in Fig. 1, this hybrid device relies on the use of two energy conversion devices: the photovoltaic cell that converts solar energy into electricity and the thermoelectric generator that converts thermal energy into electricity. In this work, we consider photovoltaic-thermoelectric devices that are thermally coupled (direct thermal contact) and electrically isolated (4-terminal configuration). In this section, we present a multiphysics model built as a predictive tool of the performances of the PVC-TEG device and taking into account the coupling between optical, thermal and electrical effects. As shown in Fig. 2, the hybrid device is divided into two sub-systems (the PVC and the TEG), each described by its own multiphysics model, and thermally coupled through a model of the thermal transport in the hybrid device. The final outputs of the model are the electrical powers generated by the PVC and the TEG. In the following subsections, we describe the physical models used for the two sub-systems as well as the model used to describe the thermal transport. We then validate quantitatively our model by comparison with an existing model from the literature.

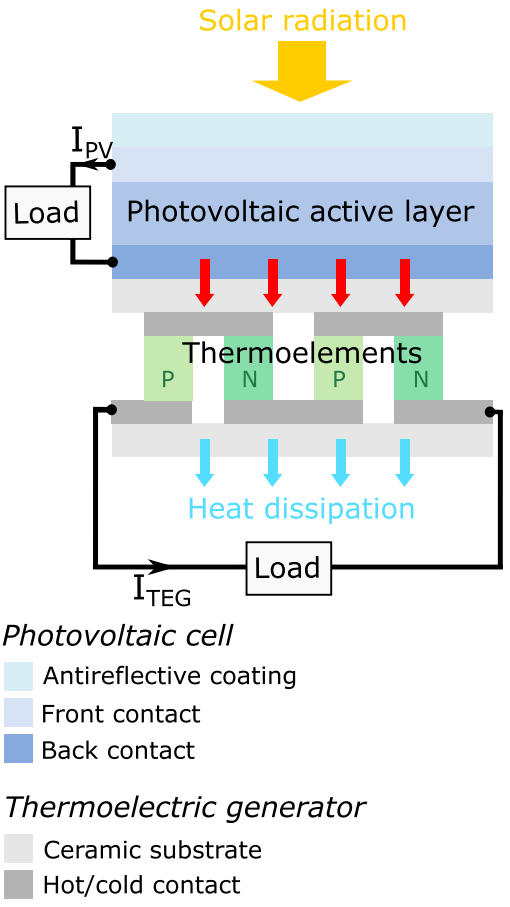

Fig. 1. Schematic of a thermally coupled photovoltaic-thermoelectric hybrid device, combining a photovoltaic cell (PVC) and a thermoelectric generator (TEG) in a 4-terminal configuration.

2.1. Model of the photovoltaic cell

Our approach is to model the PVC with the fewest material parameters possible and to improve the optical model of the PVC, compared to existing PVC-TEG models, by implementing a spectrally-dependent response for all the layers. Thus, the electrical properties of the PVC, and in particular their evolution as a function of temperature, are only accounted for in the calculation of the conversion efficiency, as detailed in the following. Refining the model would require to implement electrical transport equations using additional material parameters such as the doping values and carrier mobilities.

In the model, a PVC is represented by a stack of layers, defined by their complex refractive indices and by their thicknesses, including the active layer in which the photovoltaic conversion takes place. The open-source code *Moosh* [22] is used to simulate the interaction between the incident unpolarized solar illumination at normal incidence and the PVC, considering reflection and absorption phenomena at each layer. The thermal radiation, on the other hand, is taken into account in the thermal model described in subsection 2.3. *Moosh* allows to calculate the absorbed radiation power density $p_{abs}^{layer}(\lambda)$ in each layer of the PVC, as well as the total radiation power densities transmitted $p_{trans}^{PV}(\lambda)$ and reflected $p_{refl}^{PV}(\lambda)$ by the PVC. For the sake of simplicity, and to reduce the amount of input data required to run the model, we did not take into account the impact of temperature on the optical properties of the materials, but rather used the refractive index values at ambient temperature.

For all layers except the active layer, the absorbed radiation power density p_{abs}^{layer} is used to determine the generated heat power density q^{layer}

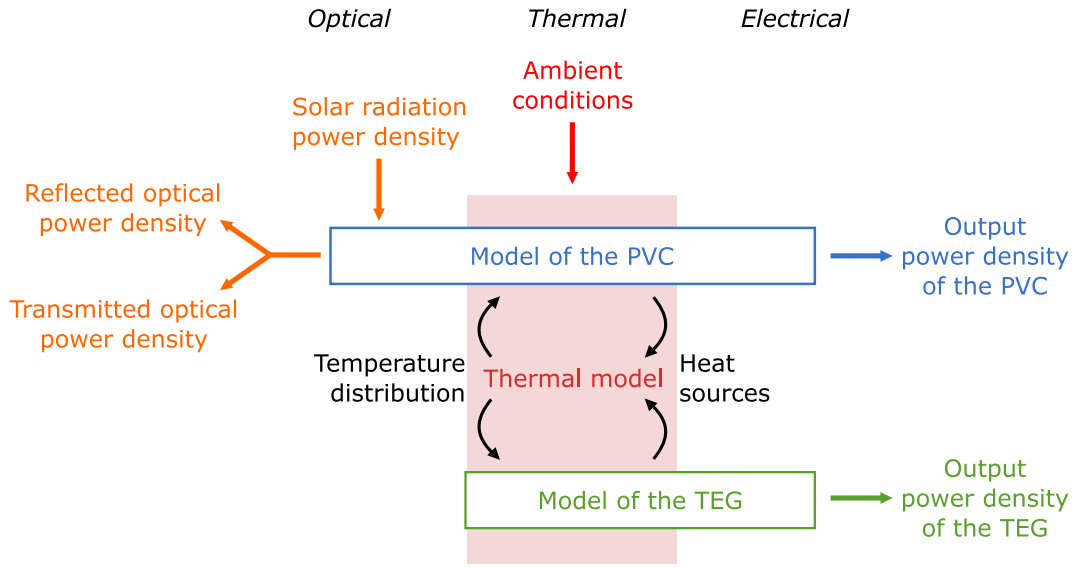

Fig. 2. Principle of the proposed multiphysics model: the photovoltaic-thermoelectric device is modeled as two sub-systems (photovoltaic cell and thermoelectric generator) thermally coupled through a model of the thermal transport in the hybrid device.

assuming that all optical absorption leads to heat generation ($q^{layer} = p_{abs}^{layer}$).

As for the active layer of the photovoltaic cell, several physical phenomena are at play in the conversion of the absorbed radiation power density p_{abs}^{PV}:

- Photovoltaic conversion, generating the electrical power density $p_{out}^{PV}(T)$;
- Radiative recombination, i.e direct recombination of photogenerated electron-hole pairs that can result in photon emission outside the layer, generating the radiation power density $p_{rad}(T)$;
- Thermalization, i.e non-radiative relaxation of photogenerated electron-hole pairs with an energy above the band gap E_g of the photovoltaic absorbing material, giving rise to a heat power density $q_{therm}(T)$;
- Non-radiative losses, including non-radiative recombination of excitons and Joule heating, collectively generating the heat power density $q_{NRad}(T)$.

As a consequence, the radiation power density absorbed in the PV active layer p_{abs}^{PV} can be expressed as:

$$p_{abs}^{PV} = p_{out}^{PV}(T) + p_{rad}(T) + q_{therm}(T) + q_{NRad}(T) \quad (1)$$

The heat power density generated in the active layer $q^{PV}(T)$ results from the combination of thermalization and non-radiative losses: $q^{PV}(T) = q_{therm}(T) + q_{NRad}(T)$. As for radiative losses (p_{rad}), in the case of conventional photovoltaic absorbers such as Si or GaAs, they represent a negligible part of the incident solar power ($\approx 0.1\%$) [23]. Thus, we assume that all the radiation power that is absorbed in the active layer and not converted into electricity generates heat, i.e:

$$q^{PV}(T) = p_{abs}^{PV} - p_{out}^{PV}(T) \quad (2)$$

It should be noted that both the output electrical power density p_{out}^{PV} of the cell and the heat generated q^{PV} in the active layer depend on the PVC temperature T. This coupling adds complexity to the calculation of the final temperature distribution in the system, increasing computing time.

The output electrical power density of the cell p_{out}^{PV} is calculated using a simple empirical model. The conversion efficiency of photovoltaic cells is conventionally measured in Standard Test Conditions, under illumination by the AM1.5G solar spectrum at 1000 W.m^{-2} and at a controlled temperature T_{ref} of 25 °C. However, as described previously, in normal operating conditions, a photovoltaic cell heats up due to thermalization of high-energy carriers and non-radiative losses, reaching up to around 60 °C [24,25]. In order to describe the impact of the temperature T on conversion efficiency η of a PVC, we use a linear model, as presented in detail in Ref.[26]:

$$\eta(T) = \eta_{ref} + \beta(T - T_{ref}) \quad (3)$$

where η_{ref} is the reference conversion efficiency of the PVC, measured in the Standard Test Conditions. β is the solar cell's temperature coefficient of efficiency, which characterizes the variation of conversion efficiency with increasing temperature. Eq. (3) is used here to calculate the conversion efficiency of the PVC at a given temperature T and can be adjusted or replaced in the case of an illumination different from AM1.5G.

The electrical power density generated by the PVC at temperature T is then given by:

$$p_{out}^{PV}(T) = \eta(T) \cdot \int_{\lambda_{min}}^{\lambda_{max}} p_{sun}(\lambda) d\lambda \quad (4)$$

where $p_{sun}(\lambda)$ is the spectral radiation power density of the AM1.5G solar spectrum, and λ_{min} and λ_{max} are its lower and upper limits respectively.

The inputs and outputs of the model for the photovoltaic cell are summarized in Table 1. In our model, the electrical power density p_{out}^{PV} is

Table 1
Summary of the inputs and outputs of the model for the photovoltaic cell.

Category	List of inputs/outputs
Inputs	Composition of the stack (refractive indices, thicknesses) Incident solar spectral radiation power density $p_{sun}(\lambda)$ (W.m^{-2}.nm^{-1}) Reference efficiency of the cell η_{ref} Reference temperature of the cell T_{ref} (K) Temperature coefficient of efficiency β (K^{-1}) Temperature of the active layer T (K)
Outputs	Electrical power density generated by the PV cell p_{out}^{PV} (W.m^{-2}) Heat power density generated in each layer q^{layer} (W.m^{-2}) Heat power density generated in the active layer q^{PV} (W.m^{-2}) Spectral radiation power density transmitted through the PV cell $p_{trans}^{PV}(\lambda)$ (W.m^{-2}.nm^{-1}) Spectral radiation power density reflected by the PV cell $p_{refl}^{PV}(\lambda)$ (W.m^{-2}.nm^{-1})

used to characterize the performances of the PVC but also to calculate the heat power density generated in the active layer q^{PV} using Eq. (2).

In the case of a PVC-TEG device with a photothermal interface (see subsection 3.1), the radiation power density $p^{PV}_{trans}(\lambda)$ transmitted by the PVC is used as the radiation power density incident on the photothermal interface.

2.2. Model of the thermoelectric generator

The TEG consists of a stack of layers representing its usual components: ceramic substrates, metallic contacts and thermoelectric layer, as illustrated in Fig. 1. The active layer of the TEG, that we call the thermoelectric layer, is made of an array of N pairs of n- and p- doped thermoelectric legs. All thermoelectric legs are assumed to have the same properties: length L_{leg}, cross-section A_{leg}, thermal conductivity κ_{leg}, electrical resistivity ρ_{leg}, Seebeck coefficient α_{leg}. The density of pairs of thermoelectric elements by unit surface d is given by the ratio N/S_{TEG}, with S_{TEG} the total surface of the TEG. We use the parameters of TEGs with finite surface as input, as these data are usually provided by manufacturers. However, the outputs are calculated as electrical and heat power densities in Eqs. (8)–(11) to describe TEGs with infinite surface. The equations describing the physical behavior of a TEG presented in this section are taken from previous works [27,28].

The thermal conductivity of the thermoelectric layer κ_{TE} reads:

$$\kappa_{TE} = 2d \cdot A_{leg} \cdot \kappa_{leg} \tag{5}$$

A TEG connected to a load resistance R_L generates electric current when a temperature difference is present between the hot side (at temperature T_H) and the cold side (at temperature T_C) of the thermoelectric elements. This current depends on the internal electric resistance R_{leg} and Seebeck coefficient α_{leg} of a single leg, according to:

$$I = \frac{2N \cdot \alpha_{leg}(T_H - T_C)}{2N \cdot R_{leg} + R_L} \tag{6}$$

with:

$$R_{leg} = \frac{\rho_{leg} \cdot L_{leg}}{A_{leg}} \tag{7}$$

We can then calculate the electrical output power density generated by the TEG using:

$$p^{TEG}_{out} = \frac{I^2 \cdot R_L}{S_{TEG}} \tag{8}$$

Note that the maximum power output is achieved when the load resistance matches the internal resistance of the TEG ($R_L = 2N \cdot R_{leg}$), which is the condition we set in the model.

The current flowing through the operating TEG is also responsible for heat generation inside the thermoelectric layer by Joule effect, which is described by:

$$q^{TE}_{Joule} = \frac{2I^2 \cdot N \cdot R_{leg}}{S_{TEG}} \tag{9}$$

Furthermore, because a TEG is also a Peltier module, Peltier effect occurs at the top and bottom interfaces of the thermoelectric layer, heating the cold side and cooling down the hot side. The heat power density generated by Peltier effect at the hot and cold interfaces, respectively designated as $q^{H}_{Peltier}$ and $q^{C}_{Peltier}$ can be calculated using

$$q^{H}_{Peltier} = -2\,d \cdot \alpha_{leg} \cdot T_H \cdot I \tag{10}$$

$$q^{C}_{Peltier} = 2\,d \cdot \alpha_{leg} \cdot T_C \cdot I \tag{11}$$

The heat power densities calculated using Eqs. (9)–(11) are used in the thermal transfer model described in the subsection 2.3, in order to determine the temperature at each interface of the PVC-TEG device. The inputs and outputs of the model for the thermoelectric generator are summarized in Table 2.

2.3. Thermal model of the PVC-TEG device

The thermal transport in the PVC-TEG device is modeled by using a one-dimensional model and assuming the steady-state. As depicted in Fig. 3, the whole device is represented as a stack of n layers with infinite surface, each layer i being characterized by its own thickness e_i and thermal conductivity κ_i. All the layers in the stack are in thermal contact with the adjacent layers, allowing conductive thermal transfer. In this model, the thermal contact resistances of the different interfaces are neglected. The top and bottom layers are also in contact with the environment, which is air at ambient temperature T_{amb}, resulting in convective and radiative thermal transfer. Furthermore, the model accounts for heat power densities that can be generated inside the layers or at the interfaces, due to various physical phenomena that have been described previously (thermalization in the PVC, Joule and Peltier effects in the TEG, …). The equations of thermal transport presented in this section allow to calculate the temperature at each interface of the system (T_k, k from 1 to n), knowing the properties of each layer i (thickness e_i, thermal conductivity κ_i, generated heat power density q_i) and the properties of the top and bottom interfaces (emissivity ϵ_{top} or ϵ_{bottom}, convective heat transfer coefficient h_{top} or h_{bottom} and T_{amb}).

Let us consider the general case of an inner interface k located between two layers ($i-1$ and i) of the device. As shown in Fig. 3, the temperature T_k of the interface k depends on the conduction from the layers above ($i-1$) and below (i), as well as on the heat power densities generated in these layers (q_{i-1} and q_i) and eventually at the interface itself (q^{int}_k). Note that, in our model, the only source of interfacial heat generation is the Peltier effect around the thermoelectric layer of the TEG (Eqs. 10,11). Heat transfer by conduction is described using the Fourier law: $\overrightarrow{\phi_{cd}} = -\kappa_{th}\overrightarrow{\nabla}T$. Assuming that the heat generated in each layer is delivered at a point source in the middle of the layer, the general heat balance equation for the interface k can be written as:

$$\frac{\kappa_{i-1}}{e_{i-1}}(T_k - T_{k-1}) + \frac{\kappa_i}{e_i}(T_k - T_{k+1}) = q^{int}_k + \frac{q_{i-1}}{2} + \frac{q_i}{2} \tag{12}$$

where κ_{i-1} and e_{i-1} are the thermal conductivity and thickness of the layer above the interface, while κ_i and e_i are the thermal conductivity and thickness of the layer below. T_{k-1} and T_{k+1} are the temperatures of the surrounding interfaces.

As for the outer interfaces of the device, heat transfer by convection and radiation toward the environment should be taken into account. Each interface is defined by its convective heat transfer coefficient (h_{top}

Table 2
Summary of the inputs and outputs of the model for the thermoelectric generator.

Category	List of inputs/outputs
Inputs	Absolute Seebeck coefficient of a single TE leg α_{leg} (V.K^{-1}) Thermal conductivity of a single TE leg κ_{leg} (W.m^{-1}.K^{-1}) Electrical resistivity of a single TE leg ρ_{leg} (Ω.m) Length of a single TE leg L_{leg} (m) Cross-section of a single TE leg A_{leg} (m^2) Number of pairs of TE legs N Total surface of the TEG S_{TEG} (m^2) Load resistance R_L (Ω) Temperature of the hot T_H and cold T_C contacts (K)
Outputs	Electrical power density generated by the TEG p^{TEG}_{out} (W.m^{-2}) Heat power density generated by Joule effect in the TE layer q^{TE}_{Joule} (W.m^{-2}) Heat power density generated at the hot $q^{H}_{Peltier}$ side of the TE layer by Peltier effect (W.m^{-2}) Heat power density generated at the cold $q^{C}_{Peltier}$ side of the TE layer by Peltier effect (W.m^{-2})

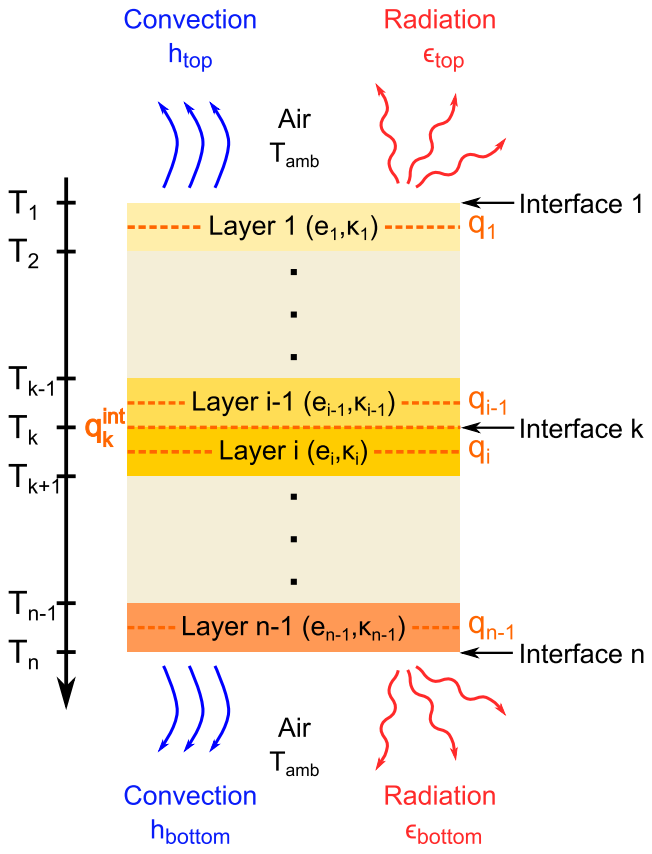

Fig. 3. Schematic of the one-dimensional thermal model of the PVC-TEG device. Each layer i is characterized by its thickness e_i, its thermal conductivity κ_i and the heat power density generated inside q_i. Each interface k is represented by its temperature T_k and the heat power density generated at the interface q_k^{int}.

or h_{bottom}, in W.m^{-2}.K^{-1}) and its total hemispherical emissivity (ϵ_{top} or ϵ_{bottom}). The thermal power density exchanged by convection between one of the outer interfaces and the environment is given by: $\phi_{cv} = h(T - T_{amb})$. The radiative thermal exchange is expressed using Stefan–Boltzmann's law: $\phi_{rad} = \epsilon \cdot \sigma (T^4 - T_{amb}^4)$, where σ is the Stefan–Boltzmann constant. Emissivity is an intrinsic property of the material composing the interface, and it is assumed that the top and bottom layers are opaque in the range covered by the Planck function at the temperatures considered. The convective heat transfer coefficient is usually an experimental value depending on the geometry and position of the interface, and on environmental conditions such as wind speed.

In the case of the top interface (interface 1), the heat balance can thus be written as:

$$\frac{\kappa_1}{e_1}(T_1 - T_2) + h_{top}(T_1 - T_{amb}) + \epsilon_{top} \cdot \sigma (T_1^4 - T_{amb}^4) = \frac{q_1}{2} \quad (13)$$

Likewise, the heat balance equation for the bottom interface (interface n) is given by:

$$\frac{\kappa_{n-1}}{e_{n-1}}(T_{n-1} - T_n) + h_{bottom}(T_n - T_{amb}) + \epsilon_{bottom} \cdot \sigma (T_n^4 - T_{amb}^4) = \frac{q_{n-1}}{2} \quad (14)$$

In order to solve these heat transport equations (Eqs. (12)–(14)) and calculate the temperature at each interface (T_k, k from 1 to n), it is necessary to know the different heat power densities (q_i and q_k^{int}) generated in the device. It includes the heat power density generated in the PVC (q^{layer} and q^{PV}) and the heat power densities generated in the TEG (q_{Joule}^{TE}) and at the top and bottom interfaces of the TEG ($q_{Peltier}^{H}$ and $q_{Peltier}^{C}$) as described in the subsections 2.1 and 2.2. Table 3 summarizes the inputs and outputs of the thermal transport model used for the PVC-TEG device.

Table 3
Summary of the inputs and outputs of the model for the thermal transport in the PVC-TEG device.

Category	List of inputs/outputs
Inputs	Thermal conductivity of each layer κ_i (W.m^{-1}.K^{-1}) Thickness of each layer e_i (m) Heat power density generated in each layer q_i (W.m^{-2}) Heat power density generated at each interface q_k^{int} (W.m^{-2}) Emissivity of the top (ϵ_{top}) and bottom (ϵ_{bottom}) interfaces Convective heat transfer coefficient at the top (h_{top}) and bottom (h_{bottom}) interfaces (W.m^{-2}.K^{-1}) Ambient temperature T_{amb} (K)
Outputs	Temperature at each interface of the system T_k (K)

2.4. Validation of the PVC-TEG model by comparison with literature

The purpose of this subsection is to quantitatively compare the results achieved with our multiphysics modeling tool on a PVC-TEG device to the results of a model from the literature. It should be noted that, while a few models of PVC-TEG devices were reported in the literature [16,29,21], offering opportunities for comparison with our model, most of these works do not provide the data required to reproduce their results. We chose the study published in 2018 by Zhou et al. [30], as most of the input data is available in the paper. In that work, the authors describe a multiphysics model of a PVC-TEG device made of a silicon solar cell, a thermoelectric generator and a passive heat sink.

As illustrated in Fig. 4, Zhou et al. modeled two different architectures for the PVC-TEG device:

- A structure called *traditional* (see Fig. 4A), in which the PV cell layers are, from top to bottom: glass, EVA (ethylene vinyl acetate), PV active layer, EVA and tedlar. A TEG made of ceramic, copper contacts, thermoelectric elements, copper contacts and ceramic is placed just below the PVC.
- A structure called *optimized* (see Fig. 4B), designed to enhance the thermal contact between the PVC and the TEG. In this configuration, the PV cell layers are, from top to bottom: glass, EVA and PVC active layer. The top and bottom ceramic substrates of the TEG, having low thermal conductivity, are replaced by silicone layers.

In order to investigate the two PVC-TEG architectures using our modeling tool, we made some modifications with respect to the model used by Zhou et al. In the work of Zhou et al., the solar cell is covered by a nanostructured array encapsulated in an EVA layer, whose purpose is to reduce reflection at the air-PVC interface, and whose radiative properties are simulated using a Finite Difference Time Domain method. In our case, this nanostructured antireflective layer is replaced by a simple EVA layer with no optical reflection. Furthermore, it is assumed by Zhou et al. that all the radiation power reaching the active layer of the PVC is either converted into electricity or into heat, with no transmission. We thereby modified Eq. (2) to convert the radiation transmitted through the cell into heat within the active layer, as follows:

$$q^{PV} = p_{abs}^{PV} + p_{trans}^{PV} - p_{out}^{PV}(T) \quad (15)$$

where p_{trans}^{PV} is the radiation power density transmitted through the PVC, calculated using *Moosh* software as described previously in subsection 2.1.

In addition, the model used in Ref. [30] for the PVC is more complex than ours, and requires in particular the input of the doping characteristics of the different layers to determine the output power of the PVC. As described in subsection 2.1, our model uses a simple linear assumption to calculate the output power density from the values of the reference efficiency η_{ref} and temperature coefficient of efficiency β. Using the data from Ref. [30], we were able to determine that the PVC they used had an efficiency of 11.55 % at 120 °C and a temperature coefficient of −0.056

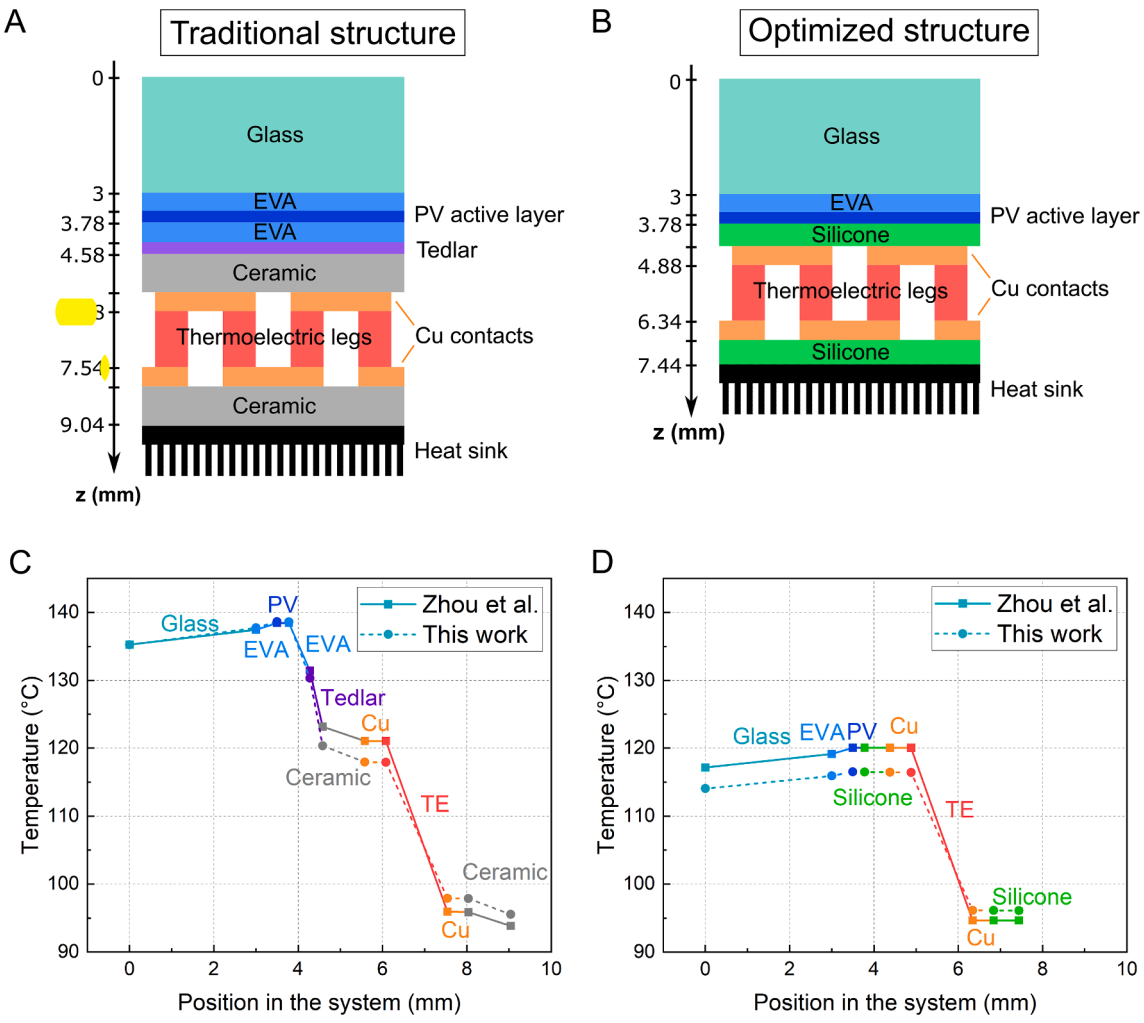

Fig. 4. (A,B) Traditional and Optimized PVC-TEG architectures proposed by Zhou et al. [30]. (C,D) Comparison of the temperature distribution obtained by Zhou et al. (plain line) and calculated using the multiphysics model presented in this work (dashed line).

%/°C, and we could thus deduce the output power density of the PVC $p_{out}^{PV}(T)$ at any temperature T using Eq. (4).

As for the TEG, no modifications were made to the model used by Zhou et al. as it is the same as ours. Most inputs of the PVC-TEG device, such as the values of the thickness and thermal conductivity of the different layers, and the parameters of the TEG, are taken directly from their publication. The ambient temperature is set at 300 K, and the incident solar radiation power density is the AM1.5G solar spectrum with a concentration ratio of 10. However, the emissivity and convection coefficients are not provided in the paper. In our model, $\epsilon_{top} = 0.85$ (for glass), $\epsilon_{bottom} = 0.1$ (for aluminum heatsink) are taken from the literature [31], and h_{top}, h_{bottom} values are adjusted within consistent ranges (1–10 W.m^{-2}.K^{-1} for h_{top}; 50–200 W.m^{-2}.K^{-1} for h_{bottom}). h_{bottom} is used to model the properties of the heat sink of the model of Zhou et al. All the parameters used for the calculations presented in Figs. 4C-D are supplied in the Supporting information in Table S1 and Fig. S1 (permittivity of the different materials).

Fig. 4 displays the temperature distribution along the two PVC-TEG devices (*traditional* and *optimized*), calculated using our modeling tool, compared to the results of Zhou et al. For both structures, our model shows a good agreement with the calculations from Zhou et al. The main difference is a lower temperature gradient through the thermoelectric layer in our case, probably due to a mismatch in the thermal conductivity of the TE layer (all other thermal conductivities being equal to those of Zhou et al.). A difference of h_{top} and h_{bottom} between this work et Zhou's could also partially explain the discrepancies, as well as could an underestimation of the heat generated in the PV cell.

Furthermore, we have calculated the output power densities of the PVC and TEG resulting from these temperature distributions as presented in Table 4. For both structures, the output power density of the PV cell is in agreement with the results from Zhou et al., which is consistent with the similar temperature values obtained in both cases for the PVC. The output power density of the TEG calculated with our model is lower than the value of Zhou et al. in both traditional and optimized structures, due to the lower temperature difference through the thermoelectric layer. For instance, in the case of the *traditional* structure, Zhou et al. calculated a difference of 25.1°C, whereas ours is only 21.9 °C. Yet, overall, the results of our PVC-TEG model are in good quantitative agreement with Ref. [30] (less than 5 % of relative error on the

Table 4
Comparison of the output power densities of the PVC-TEG device calculated by our model and that of Zhou et al., for the *traditional* and *optimized* structures.

Output power density (W.m^{-2})	PVC	TEG	PVC-TEG device
Traditional structure			
Zhou et al.	1051.6	112.0	1163.6
This work	1043.5	71.2	1114.7
Optimized structure			
Zhou et al.	1154.5	114.5	1269.0
This work	1166.4	73.2	1239.6

value of the output power density of the PVC-TEG device).

3. Integrating a photothermal interface

3.1. Model of the photothermal interface

In this section, we present the model used for the photothermal interface. Similarly to the PVC, the photothermal interface is represented by a stack of layers, one of which being photothermally active. The model is meant to simulate any kind of multilayered photothermal interface. For example, Fig. 5 shows a PTI made of a photothermal layer on top of a multilayered substrate, covered by an encapsulating material. The PTI is then optically and thermally coupled with the PVC and TEG as described in subsection 3.2.

The PTI is only defined by the structure of the stack (thermal conductivity and thickness of the different layers) and its spectral absorptance $A(\lambda)$. The absorptance spectrum can be determined through various methods, experimental or computational, depending on the user's preferences and available tools, and is used to calculate the radiation power density p_{abs}^{PTI} absorbed by the PTI under an incident spectral radiation power density $p_{inc}(\lambda)$:

$$p_{abs}^{PTI} = \int_{\lambda_{min}}^{\lambda_{max}} A(\lambda) \cdot p_{inc}(\lambda) d\lambda \tag{16}$$

where λ_{min} and λ_{max} are the lower and upper limits of the incident spectrum.

In the case of a complete PVC-PTI-TEG system, $p_{inc}(\lambda)$ is the spectral radiation power density transmitted by the PV cell ($p_{trans}^{PV}(\lambda)$), as calculated in subsection 2.1.

The next step is to calculate the heat power density q^{PTI} generated by the photothermal interface, assuming that the absorbed radiation power density is fully converted into heat: $q^{PTI}=p_{abs}^{PTI}$. In the thermal model (see subsection 2.3), the heat power density q^{PTI} is set to be generated at the center of the photothermally active layer, as shown in Fig. 5.

The inputs and outputs of the PTI model are summarized in Table 5.

3.2. Coupling of the PVC, PTI and TEG components

In order to simulate the physical behavior of a complete PVC-PTI-TEG system under illumination, it is necessary to carefully specify the coupling conditions of the three inter-dependent sub-systems.

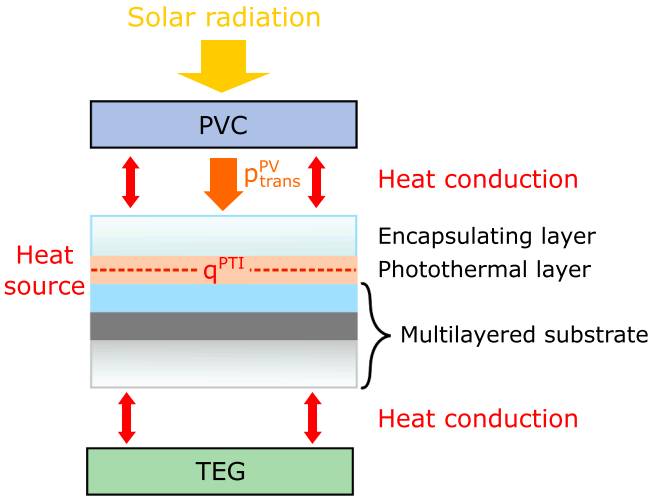

Fig. 5. Schematic of a photothermal interface as modeled in the multiphysics tool. The photothermally active layer is placed on a multilayer substrate and covered by an encapsulating material. The incident spectral radiation power density is the one transmitted by the PVC.

Table 5
Summary of the inputs and outputs of the model for the photothermal interface.

Category	List of inputs/outputs
Inputs	Refractive indices of the materials Structure (order of the layers in the stack) Thickness e^{layer} of each layer (m) Thermal conductivity κ_{layer} of each layer ($W.m^{-1}.K^{-1}$) Spectral absorptance $A(\lambda)$ of the PTI Incident spectral radiation power density $p_{inc}(\lambda)$ ($W.m^{-2}.nm^{-1}$)
Outputs	Heat power density generated in the photothermal interface q^{PTI} ($W.m^{-2}$)

The PVC, PTI and TEG are assumed to be in perfect thermal contact, allowing heat exchange between the subsystems. Thus, when it comes to thermal transfer, the top layer of the PTI is placed directly below the bottom layer of the PVC, while the bottom layer of the PTI is placed directly above the top layer of the TEG. In both cases, the interface thermal resistance is neglected and the heat transfer is assumed to be fully conductive. The equations of thermal transport described in subsection 2.3 can then be used to calculate the heat flux among the complete PVC-PTI-TEG system.

As for the solar radiation transfer, we only consider transmission from the PVC to the PTI, by assuming that the light transmitted through the PVC is the incident spectral radiation power density in the PTI model. Thus, in our coupled setting, no optical power is emitted from the PTI toward the PVC nor the TEG. Rather, all the optical power that is reaching the PTI and is not absorbed (i.e. the reflected and eventually transmitted power) is supposed to vanish from the system. This approximation is valid as long as the PTI has a high absorption coefficient, which is usually the case.

Fig. 6 presents the different steps involved in the calculation of the output power density of the PVC and the TEG in a PVC-PTI-TEG system. At the beginning of the process, the whole system is set at ambient temperature. The first step of the process consists in determining the absorptance of the PTI, as described in subsection 3.1. Then, based on the incident solar spectral radiation power density and the properties of the PVC, photonic simulations using *Moosh* software are conducted to compute the radiation power density absorbed in each layer of the cell, as well as the radiation power density transmitted through the cell. The latter is then used to calculate the radiation power density absorbed by the PTI based on its spectral absorptance. The heat generated in the PVC, PTI and TEG can finally be calculated using the models presented respectively in subsections 2.1, 3.1 and 2.2.

The system of equations coupling the temperature at each interface to the heat generated in each layer (Eq. (2), Eqs. (9)–(14)) is solved using *MatLab*. The new set of temperatures is then used to actualize the heat power densities generated within the stack. Through an iterative process, the solver converges towards a set of positive solutions, which are used to calculate the electrical power density generated by the PVC and the TEG using respectively Eq. (4) and Eq. (8).

3.3. Validation of the PVC-PTI-TEG model by comparison with literature

Our multiphysics model showed that it is consistent with previously published PVC-TEG models. The next challenge consists in confirming its capabilities to predict the behavior of a real operating PVC-TEG device integrating a photothermal interface. In this section, we compare the simulation results of our multiphysics model with the experimental findings reported by Park et al. in their article published in 2020 [10]. They investigated the impact of different interfaces on the performance of a photovoltaic-thermoelectric device. Three distinct PVC-TEG devices were fabricated, wherein the PVC and the thermoelectric generator are identical, differing only by the nature of the interface between them. The interfaces studied were 1 mm thick and composed of either air, boron nitride (BN), or boron nitride loaded with reduced graphene oxide (BN-

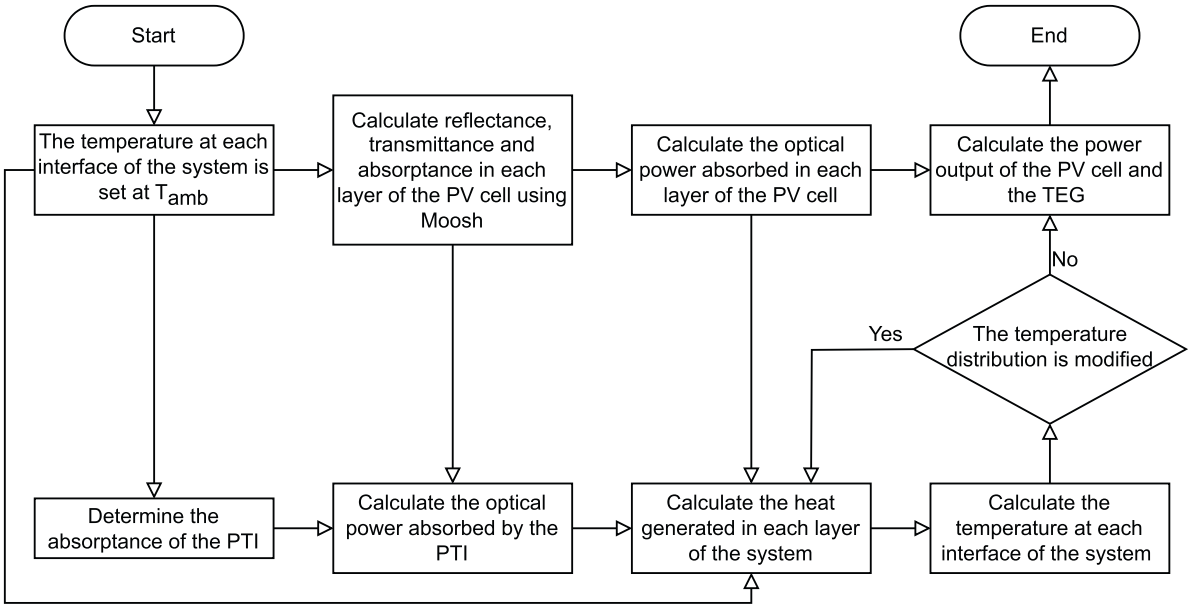

Fig. 6. Principle of the multiphysics tool allowing to calculate the electrical power density generated by a PVC-PTI-TEG device based on the properties of its components.

rGO). Temperature distribution within the system under solar illumination was measured using four thermocouples placed respectively: (1) above and (2) below the PVC, and (3) above and (4) below the TEG.

The experimental temperature distribution data provided an excellent basis for comparison with our simulation results. Our objective was to model the experimental systems described by Park et al. using our multiphysics model and compare simulation results with experimental results to assess the model's reliability. However, some necessary input data for our model were not explicitly provided in the referenced article. Therefore, we proceeded step by step, starting with simulating the optical behavior of the PV cell alone.

According to the information provided by Park et al., the PV cell consists of a 232 µm thick layer of crystalline silicon surrounded by two 76 nm thick anti-reflective layers made of silicon nitride (SiNx:H). We incorporated these parameters into our model using the refractive indices of SiNx:H and intrinsic crystalline silicon. Upon simulating the PV cell's optical behavior under solar illumination, we observed a significant deviation in absorptance spectra for wavelengths exceeding 800 nm, as can be seen in Fig. 7. This deviation was attributed to the fact that intrinsic silicon does not absorb photons with energies below the bandgap, whereas doped silicon, typically used in PV cells, exhibits free charge carriers resulting in sub-bandgap absorption [32,33].

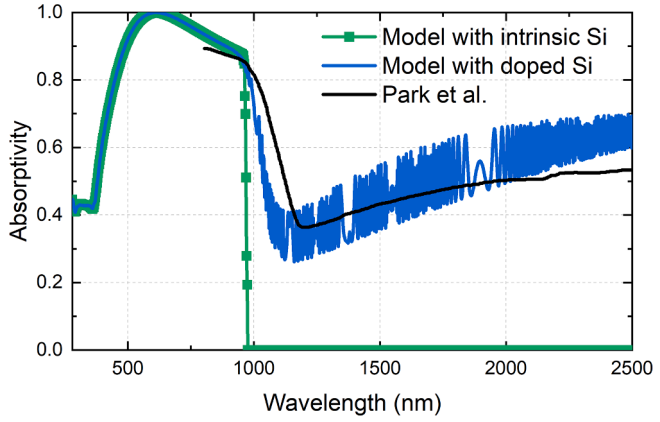

Fig. 7. Absorptance of a c-Si PVC measured by Park et al. [10] (black line), and calculated using *Moosh* for intrinsic c-Si (green line, square markers) and doped Si (blue line). (For interpretation of the references to colour in this figure legend, the reader is referred to the web version of this article.)

To overcome this limitation, we modified the refractive index used for silicon by incorporating the effect of free carriers using the empirical formula proposed by Green [34,35]. By selecting a doping concentration n of 3.3×10^{20} cm^{-3} and p of 1×10^{16} cm^{-3}, the simulated absorptance spectrum closely matched the experimental data (see blue and black lines in Fig. 7), underscoring the importance of the doping concentration for accurately simulating the PVC behavior.

Once the optical properties of the PVC had been adjusted, the remaining inputs were set. We used the same TEG properties as in the previous section due to their similarity to those described in Park's article [10]. The interface layer thickness (1 mm) and thermal conductivity of BN and BN-rGO (65 W/m·K) were sourced from Park's paper. For the calculation of the optical power absorbed by the photothermal interface (air or BN-rGO), the absorptance of the PTI is determined from the experimental data reported by Park et al. Although not explicitly stated in the article, we assumed passive heat dissipation at the bottom of the device with a convection coefficient of 20 $W.m^{-2}.K^{-1}$, and a top surface convective coefficient of 5 $W.m^{-2}.K^{-1}$.

Subsequently, as displayed in Fig. 8, we compared the calculated temperature distribution under solar illumination with experimental results for systems without an interface (air, A) and with a BN-rGO interface (B). While simulation data closely matched experimental observations for the system without an interface (see Fig. 8A), significant discrepancies were noted for the system with the BN-rGO interface. To address this, we introduced a new parameter into our simulations: the interface thermal resistance, which can strongly impact the temperature distribution and output power of a PVC-TEG device [36].

Previous simulations assumed perfect thermal contact between each layer, which is not the case in real-world devices. To take into account the effect of interface thermal resistance R_{int}^{th}, the model of thermal transport was modified by adding, at each interface within the PVC-PTI-TEG system, a layer with a thickness e_{int} of 1 nm and a thermal conductivity of κ_{int}, defined as:

$$\kappa_{int} = \frac{e_{int}}{R_{int}^{th}} \tag{17}$$

As can be seen in red and circle markers in Fig. 8, the addition of a thermal resistance of 3×10^{-3} $m^2.K.W^{-1}$ at each interface significantly

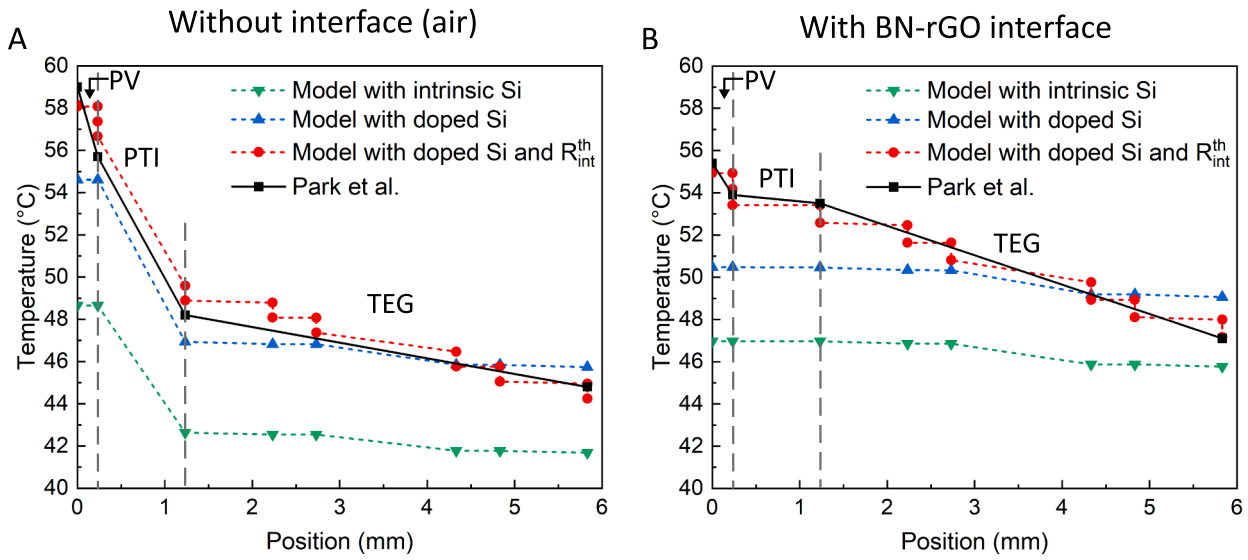

Fig. 8. Temperature distributions within a PVC-TEG device (A) without interface and (B) with a BN-rGO photothermal interface. The black lines and square markers represent the temperature experimentally measured by Park et al. [10]. The dashed lines show the results obtained by the multiphysics model with intrinsic c-Si and no interface thermal resistance (green, down-pointing triangle), with doped c-Si and no interface thermal resistance (blue, up-pointing triangle), and with doped c-Si and a interface thermal resistance of 2×10^{-3} $m^2.K.W^{-1}$ between each layer (in red, circle). (For interpretation of the references to colour in this figure legend, the reader is referred to the web version of this article.)

improved the agreement between simulations and experimental data, especially in the case of BN-rGO interface.

These results highlight the initial limitations of our multiphysics tool, which did not take into account the doping concentration of the PVC active layer or the interface thermal resistance. Both parameters strongly impact the model's prediction, and should thus be precisely known when simulating a real device. However, the versatility of our tool was also evidenced, as it can be easily modified to overcome these limitations.

4. Conclusion

In this study, a novel modeling tool has been proposed to predict the performances of PVC-TEG hybrid devices. This multi-physics tool allows to calculate the temperature distribution within the device under solar illumination, as well as its electrical output power, based on the coupling between optical, electrical and thermal effects. Notably, the multi-physics model takes into account the spectral dependence of optical properties for all layers constituting the photovoltaic cell, allowing a more detailed calculation and spatial positioning of the heat power sources. Another novelty of the model proposed is to implement a photothermal interface, as the use of such interfaces between the solar cell and the thermoelectric generator is a rising strategy to exploit the near infrared photons and boost the output power of the thermoelectric component.

The results obtained with the multi-physics tool are in agreement with a previous model from the literature, and were also validated against experimental data, after refining the model with some additional parameters. In particular, the model is sensitive to the doping of the photovoltaic active layer, as well as the interface thermal resistances.

The multi-physics model presented in this study is a versatile tool for calculating the output power of PVC-TEG hybrid devices, with or without a photothermal interface, under various environmental conditions. It may, in particular, be utilized to guide the design of an optimal photothermal interface for a specific PVC-TEG couple, in order to achieve the highest global output power for the hybrid device.

CRediT authorship contribution statement

Sébastien Hanauer: Writing – review & editing, Writing – original draft, Visualization, Validation, Software, Methodology, Investigation, Formal-analysis, Conceptualization. **Léopold Boudier:** Writing – review & editing, Writing – original draft, Investigation. **Adnen Mlayah:** Writing – review & editing, Supervision. **Inès Revol:** Writing – review & editing, Writing – original draft, Visualization, Supervision, Project administration, Funding acquisition, Conceptualization.

Declaration of competing interest

The authors declare the following financial interests/personal relationships which may be considered as potential competing interests: Ines Revol reports financial support was provided by French National Research Agency. If there are other authors, they declare that they have no known competing financial interests or personal relationships that could have appeared to influence the work reported in this paper.

Data availability

All the parameters used in our simulations are provided either in the text or the Supplementary Information.

Acknowledgements

The authors acknowledge the support of this work by the French National Research Agency under grant ANR-21-CE50-0003 (project HYDRES). The authors also thank Ihar Faniayeu and Alexandre Dmitriev for their collaboration, as well as Rodolphe Vaillon for his insightful advices.

Appendix A. Supplementary data

Supplementary data associated with this article can be found, in the online version, at https://doi.org/10.1016/j.ecmx.2024.100665.

References

[1] Wang N, Han L, He H, Park N-H, Koumoto K. A novel high-performance photovoltaic–thermoelectric hybrid device. Energy Environ Sci 2011;4(9):3676.
[2] Park K-T, Shin S-M, Tazebay AS, Um H-D, Jung J-Y, Jee S-W, et al. Lossless hybridization between photovoltaic and thermoelectric devices. Scientific Rep 2013;3(1):2123.
[3] Zhang Y, Fang J, He C, Yan H, Wei Z, Li Y. Integrated energy-harvesting system by combining the advantages of polymer solar cells and thermoelectric devices. J Phys Chem C 2013;117(47):24685–91.
[4] Hsueh T, Shieh J, Yeh Y. Hybrid Cd-free CIGS solar cell/TEG device with ZnO nanowires. Prog Photovoltaics Res Appl 2015;23(4):507–12.
[5] Lorenzi B, Mariani P, Reale A, Di Carlo A, Chen G, Narducci D. Practical development of efficient thermoelectric – photovoltaic hybrid systems based on wide-gap solar cells. Appl Energy 2021;300:117343.
[6] Kil T-H, Kim S, Jeong D-H, Geum D-M, Lee S, Jung S-J, et al. A highly-efficient, concentrating-photovoltaic/thermoelectric hybrid generator. Nano Energy 2017;37:242–7.
[7] Kim YJ, Choi H, Kim CS, Lee G, Kim S, Park J, et al. High-performance monolithic photovoltaic-thermoelectric hybrid power generator using an exothermic reactive interlayer. ACS Appl Energy Mater 2019;2(4):2381–6.
[8] Zhang J, Zhai H, Wu Z, Wang Y, Xie H, Zhang M. Enhanced performance of photovoltaic–thermoelectric coupling devices with thermal interface materials. Energy Rep 2020;6:116–22.
[9] Zhang J, Zhai H, Wu Z, Wang Y, Xie H. Experimental investigation of novel integrated photovoltaic-thermoelectric hybrid devices with enhanced performance. Sol Energy Mater Sol Cells 2020;215:110666.
[10] Park Y, Cho K, Yang S, Park T, Park S, et al. Performance of hybrid energy devices consisting of photovoltaic cells and thermoelectric generators. ACS Appl Mater Interfaces 2020;12(7):8124–9.
[11] Park Y, Cho K, Kim S. Performance prediction of hybrid energy harvesting devices using machine learning. ACS Appl Mater Interfaces 2022;14(9):11248–54.
[12] Narducci D, Bermel P, Lorenzi B, Wang N, Yazawa K. A Primer on Thermoelectric Generators. In: Hybrid and fully thermoelectric solar harvesting. Cham: Springer International Publishing; 2018. p. 11–43.
[13] Zhong H, Zhou Y, Wang C, Wan C, Koumoto K, Wang Z, et al. A perovskite solar cell-photothermal-thermoelectric tandem system for enhanced solar energy utilization. Sci Technol Adv Mater 2024;25(1).
[14] Khenfer R, Lekbir A, Rouabah Z, Meddad M, Benhadouga S, Zaoui F, et al. Experimental investigation of water-based photovoltaic/thermal-thermoelectric hybrid system: Energy, exergy, economic and environmental assessment. J Power Sources 2024;598:234151.
[15] Bjørk R, Nielsen K. The performance of a combined solar photovoltaic (PV) and thermoelectric generator (TEG) system. Sol Energy 2015;120:187–94.
[16] Teffah K, Zhang Y. Modeling and experimental research of hybrid PV-thermoelectric system for high concentrated solar energy conversion. Sol Energy 2017;157:10–9.
[17] Bjørk R, Nielsen K. The maximum theoretical performance of unconcentrated solar photovoltaic and thermoelectric generator systems. Energy Convers Manage 2018;156:264–8.
[18] Lorenzi B, Chen G. Theoretical efficiency of hybrid solar thermoelectric-photovoltaic generators. J Appl Phys 2018;124(2):024501.
[19] Gu W, Ma T, Song A, Li M, Shen L. Mathematical modelling and performance evaluation of a hybrid photovoltaic-thermoelectric system. Energy Convers Manage 2019;198:111800.
[20] Liu C, Cui YJ, Wang KF, Wang BL. Interlaminar mechanical performance of a multi-layered photovoltaic-thermoelectric hybrid device. Appl Math Model 2023;122:242–64.
[21] Zhou Y-P, Li M-J, He Y-L, Li Y-S. Multi-physics analysis: the coupling effects of nanostructures on the low concentrated black silicon photovoltaic system performances. Energy Convers Manage 2018;159:129–39.
[22] Krayzel F, Pollès R, Moreau A, Mihailovic M, Granet G. Simulation and analysis of exotic non-specular phenomena. J Eur Opt Soc - Rapid Publications 2010;5:10025.
[23] Shang A, Li X. Photovoltaic devices: opto-electro-thermal physics and modeling. Adv Mater 2017;29(8):1603492.
[24] Muzathik A. Photovoltaic modules operating temperature estimation using a simple correlation. Int J Energy Eng 2014;4(4):151–8.
[25] Odeh S, Behnia M. Improving photovoltaic module efficiency using water cooling. Heat Transfer Eng 2009;30(6):499–505.
[26] Dupré O, Vaillon R, Green MA. Thermal behavior of photovoltaic devices. Springer International Publishing; 2017. p. 29–74.
[27] Wu C. Analysis of waste-heat thermoelectric power generators. Appl Therm Eng 1996;16(1):63–9.
[28] Chen L, Gong J, Sun F, Wu C. Effect of heat transfer on the performance of thermoelectric generators. Int J Therm Sci 2002;41(1):95–9.
[29] Li G, Shittu S, Ma X, Zhao X. Comparative analysis of thermoelectric elements optimum geometry between photovoltaic-thermoelectric and solar thermoelectric. Energy 2019;171:599–610.
[30] Zhou Y-P, Li M-J, Yang W-W, He Y-L. The effect of the full-spectrum characteristics of nanostructure on the PV-TE hybrid system performances within multi-physics coupling process. Appl Energy 2018;213:169–78.
[31] The Engineering ToolBox; 2003. Surface Emissivity Coefficients. URL: www.engineeringtoolbox.com.
[32] Huang HC, Yee S, Soma M. Quantum calculations of the change of refractive index due to free carriers in silicon with nonparabolic band structure. J Appl Phys 1990;67(4):2033–9.
[33] Keevers M, Green M. Extended infrared response of silicon solar cells and the impurity photovoltaic effect. Sol Energy Mater Sol Cells 1996;41–42:195–204.
[34] Santbergen R, Van Zolingen R. The absorption factor of crystalline silicon PV cells: a numerical and experimental study. Sol Energy Mater Sol Cells 2008;92(4):432–44.
[35] Green MA. Silicon solar cells: advanced principles & practice. Sydney, Australia: Centre for Photovoltaic Devices and Systems; 1995. p. 46–8.
[36] Shittu S, Li G, Zhao X, Ma X, Akhlaghi YG, Fan Y. Comprehensive study and optimization of concentrated photovoltaic-thermoelectric considering all contact resistances. Energy Convers Manage 2020;205:112422.